Journal of Environmental Management 293 (2021) 112898

Contents lists available at ScienceDirect

Journal of Environmental Management

journal homepage: www.elsevier.com/locate/jenvman

Anchoring Al- and/or Mg-oxides to magnetic biochars for Co-uptake of arsenate and fluoride from water

Ziyi Shen [a,1], Jie Jin [a,1], Jingjing Fu [a,1], Meng Yang [a], Feihu Li [a,b,*]

[a] Collaborative Innovation Center of Atmospheric Environment and Equipment Technology, Jiangsu Key Laboratory of Atmospheric Environment Monitoring and Pollution Control, School of Environmental Science and Engineering, Nanjing University of Information Science and Technology, 219 Ningliu Road, Nanjing, 210044, China

[b] NUIST-UoR International Research Institute, Nanjing University of Information Science and Technology, 219 Ningliu Road, Nanjing, 210044, China

ARTICLE INFO

Keywords:
Adsorption
Black carbon
Magnetic separation
Nanocomposite
Regeneration

ABSTRACT

The co-occurrence of arsenic and fluoride in the water environment has led to many health concerns for living beings. Simultaneous removal of such ions is crucial to the safety of water resources, and biochar has been extensively engaged to address this issue. Here four magnetic biochars (mBCs) including pristine magnetic biochar and three aluminum (Al) and/or magnesium (Mg) oxides-anchored magnetic biochar (i.e., Al-mBC, Mg-mBC, and MgAl-mBC) were prepared via a facile pyrolysis method and then comprehensively evaluated as adsorbents for enhanced co-uptake of arsenate (As^V) and fluoride (F^-) from synthetic water. The mBC shows a high specific surface area of 205 $m^2\ g^{-1}$, which dropped to 116, 80, and 114 $m^2\ g^{-1}$ upon the anchoring of Al, Mg, and Mg + Al, respectively. Our results suggest that the adsorption of either As^V or F^- is highly pH-dependent, and pH 4–6 is the optimal range for maximum adsorption. The adsorption isotherm data indicate that the MgAl-mBC adsorbent outranks all other mBCs for co-uptake of both As^V and F^-. The adsorption capacity maxima of MgAl-mBC are 34.45, and 21.59 mg g^{-1} for As^V and F^-, respectively (pH = 5, $T = 10\ ^\circ C$), also highly outstripping other biochars reported in the literature. The magnetic feature of these mBCs enables us to fast reclaim and regenerate the exhausted adsorbents by an external magnet and dilute NaOH. The Al- and Mg-anchored mBCs are expected to be used as highly efficient adsorbents for environmental remediation of waters contaminated by both As^V and F^-.

1. Introduction

The pollution of arsenic (As) and fluorine (F) is widespread in natural surface and ground waters (Jadhav et al., 2015; Wasay et al., 1996). Co-occurrence of both arsenic and fluoride is widely found in groundwater (Kumar et al., 2020; Wang et al., 2021) and industrial wastewater, for instance, effluents from a fertilizer plant under normal operation were reported to contain 0–20 mg L^{-1} arsenic, and 0–200 mg L^{-1} fluoride (Beg et al., 1982). A variety of industrial fabrication and/or processing, such as metal plating, mining operations, fertilizer industries, tanneries, batteries, paper industries, and pesticides, generate effluents containing arsenic, fluoride, and other toxic heavy metals (Bibi et al., 2015, 2017). It has been reported that co-exposure to both As and F in drinking water supplies may result in more serious health effects and worse tissue damages to human beings compared to individual exposure to either As or F (Ma et al., 2017). World Health Organization (WHO) has regulated the maximum contaminant levels (MCL) of 10 μg L^{-1} and 1.5 mg L^{-1} for As and F, respectively. To address this issue, a wide variety of techniques have been developed in the past decades for the removal of both anions from water, including electrocoagulation (Thakur and Mondar, 2017), ionic exchange (Liu et al., 2002), membrane filtration (Xu et al., 2013), and adsorption by using lanthanum impregnated silica gel (Wasay et al., 1996), magnetic biochar (Mohan et al., 2014a), modified yak dung biochar (Luo et al., 2018), metal-organic frameworks (Haldar et al., 2020), and lanthanum-based materials (Koh et al., 2021; Merodio-Morales et al., 2020).

* Corresponding author. Collaborative Innovation Center of Atmospheric Environment and Equipment Technology, Jiangsu Key Laboratory of Atmospheric Environment Monitoring and Pollution Control, School of Environmental Science and Engineering, Nanjing University of Information Science and Technology, 219 Ningliu Road, Nanjing, 210044, China.

E-mail address: fhli@nuist.edu.cn (F. Li).

[1] These authors contributed equally to this work.

https://doi.org/10.1016/j.jenvman.2021.112898
Received 9 March 2021; Received in revised form 6 May 2021; Accepted 10 May 2021

Because of its advantages of cost efficiency, versatility, high efficiency, easy operation without any secondary pollution, adsorption has been considered one of the most promising techniques for the co-removal of both arsenic and fluoride from waters (Cuong et al., 2021; Jadhav et al., 2015). Many adsorbents have already been innovated for co-removal of both As and F. Lanthanum-anchored silica gel, for instance, was found to adsorb over 99.9% of both arsenate (As^V) and fluoride (F^-) at neutral pH from synthetic water with initial adsorptive concentrations ranging from 0.55 to 0.2 mmol L^{-1} (Wasay et al., 1996). Highly ordered mesoporous alumina and calcium-doped alumina were also reported for their superb adsorption capacities towards both As^V and F^- in solution (Daughney et al., 2011). In general, As^V and F^- have exhibited dissimilar adsorption behaviors in natural aquatic environments due to the difference in their molecular properties, it is therefore rare to find a natural mineral that shows an excellent adsorption capacity for both anions simultaneously (Jing et al., 2012). Anchoring metal oxides in porous solids has been, however, proved to be a promising strategy to this end. For example, the titanium and lanthanum oxides anchored granular activated carbon (TLAC) has simultaneous adsorption capacities of 25.1 mg As^V g^{-1} adsorbent and 17.0 mg F^- g^{-1} at pH 7 (Jing et al., 2012). It was also shown that As^V and F^- have concurrently exhibited a high affinity towards Fe and Al binary oxides (Liu et al., 2012) and (hydr)oxides (Qiao et al., 2014).

Recently, biochars derived from pyrolysis of biomass at elevated temperatures have received increasing attention for potential use as superior adsorbents in water remediation applications, for instance, contaminant management in soil and water (Ahmad et al., 2014), aqueous heavy metal removal (Inyang et al., 2016), and decontamination of wastewater (Mohan et al., 2014b; Tan et al., 2016). Several research efforts have been made to evaluate biochars as adsorbents in the removal of arsenic (Hu et al., 2015; Wang et al., 2017) and fluoride (Luo et al., 2018; Mohan et al., 2014a) from aqueous solutions. To enhance their adsorption capacities for both As^V and F^-, the pristine biochars were often modified by metal anchoring (Hu et al., 2015; Tan et al., 2016). Additionally, both Al and Mg oxides were among the superior adsorbents with high affinity to both As^V and F^- (Li et al., 2016; Purwajanti et al., 2016). However, few studies have focused on the simultaneous removal of As^V and F^- by biochar adsorbents (Kumar et al., 2020). On the other hand, magnetic nanoparticles such as Fe_3O_4 and/or γ-Fe_2O_3 were generally used as the magnet source incorporated into biochar, allowing the biochars to be fast and easily separated from solutions by an external magnetic field (Liu et al., 2017; Zhang et al., 2013). Besides, the easy and fast recovery of exhausted adsorbents will facilitate the regeneration as well as the recycling processes, making the magnetic adsorbents more cost-effective as compared to other analogous adsorbents.

In the present study, four magnetic biochars were prepared via pyrolysis of biomass (rice husk) pre-anchored with Fe, and/or Al, and/or Mg ions. The synthetic biochars were characterized by a variety of techniques and then evaluated for simultaneous adsorption of both As^V and F^- from aqueous solution at varying pH, ionic strengths, and initial adsorptive concentrations. The adsorption isotherms were studied to obtain the maximum adsorption capacity. Besides, the adsorption mechanisms were also investigated via the Schindler diagram and spectroscopic analysis. The magnetic biochars are expected to be used as highly efficient adsorbents for decontamination of wastewaters polluted by both As^V and F^-.

2. Materials and methods

2.1. Materials

Aluminum chloride hexahydrate ($AlCl_3{\cdot}6H_2O$, ≥ 97%), ferric chloride ($FeCl_3$, ≥98%), and magnesium chloride hexahydrate ($MgCl_2{\cdot}6H_2O$, ≥ 98%) were purchased from Sinopharm Chemical Reagent Co., Ltd. (Shanghai, China). Milli-Q ultrapure water (18 MΩ-cm at 25 °C) was used to prepare solutions. The As^V and F^- stock solutions (1.0 M) were prepared by dissolving a certain amount of $Na_2HAsO_4{\cdot}7H_2O$ (≥98%, JT Baker Chemical, USA) and NaF (≥98%, Sinopharm Chemical, Shanghai, China) into 100 mL of ultrapure water, respectively, and stored in a refrigerator at 4 °C for further use. All other chemicals are of A.R. grade or above unless otherwise stated.

2.2. Preparation and characterization of magnetic biochars (mBCs)

Magnetic biochars (mBCs) were prepared via the fast pyrolysis method (Zhang et al., 2013). Briefly, $FeCl_3$, $AlCl_3{\cdot}6H_2O$, $MgCl_2{\cdot}6H_2O$ were dissolved in 90 mL of ultrapure water by mass ratios of 1:0:0, 1:0:1, 1:1:0, and 1:1:1, respectively. The rice husks were immersed in the above solutions for 2 h, followed by drying in an oven at 80 °C for 24 h. The resultant mixtures were placed in a tubular furnace and pyrolyzed at 600 °C for 2 h under an N_2 atmosphere. When cooling down with the furnace to room temperature, the samples were rinsed with ultrapure water several times and dried at 80 °C for 24 h. After grinding and sieving through a 100-mesh sieve, the samples were labeled as mBC, Mg-mBC, Al-mBC, and MgAl-mBC, respectively, and stored in a desiccator for further use.

X-ray diffraction analysis of these magnetic biochar samples was conducted on an XRD-6100 diffractometer (Shimadzu, Japan) at a tube voltage of 40 kV and a tube current of 30 mA with Cu-Kα radiation (step size: 0.02°, scanning rate: 7° min^{-1}). Scanning electron micrography (SEM) was recorded using a Hitachi SU1510 microscope at an accelerating voltage of 1.5 kV. The Brunauer-Emmett-Teller (BET) surface areas were obtained by the N_2 adsorption method using a Quantachrome gas adsorption analyzer (iQ-AG-MP). Zeta (ζ) potential data were collected on a Zetasizer Nano ZS 90 apparatus (Malvern, UK). Fourier Transform Infrared Spectroscopy (FT-IR) data were collected in the wavenumber range of 4000 to 400 cm^{-1} on an Is5 infrared spectrometer (Thermo Nicolet, USA) using spectroscopic grade dried KBr (Aladdin Chemicals, Shanghai, China) as the matrix material. Before the FT-IR measurements, all the mBCs samples along with KBr were oven-dried overnight at 60 °C.

2.3. Adsorption studies

All the batch experiments were performed in triplicate at atmospheric pressure and room temperature (*ca.* 25 °C) unless otherwise mentioned. The adsorption suspensions were prepared in 15 mL polyethylene centrifuge tubes by combining adsorbents with the desired amount of As^V and/or F^- stock solution and a $NaNO_3$ solution (ionic strength (I) = 1, 10, and 100 mM), giving a total volume of 10 mL mixture with a final concentration of 1 g L^{-1} of the adsorbent. The pH was adjusted with 0.5 or 1.0 M HNO_3 and 0.5 or 1.0 M NaOH into the range of 4–11 (i.e., 4, 5, 6, 7, 8, 9, 10, and 11 ± 0.1). Then, the suspensions were bubbled with N_2 for 5 min to exclude dissolved CO_2 and equilibrated on a Lab quake tube rotator (Thermo Scientific, USA) at 60 RPM for 24 h. Finally, the supernatants were collected by centrifugation (12, 000 RPM for 15 min) and filtration with 0.45 μm PES filters (Navigator, Tianjin, China). The equilibrium concentrations of As^V and F^- in the supernatants were determined using an AFS 200T atomic fluorescence spectrometer (Tianrui, Jiangsu, China) and a JH723PC visible spectrophotometer (Jinghua, Shanghai, China), respectively. The pH values of solutions were measured using an Orion pH meter (Model 868, Thermo Scientific, USA) pre-calibrated with standard pH buffers (Leici, Shanghai, China). The amount of adsorbate adsorbed was determined from the difference between the initial and the equilibrium As^V or F^- concentrations. Adsorption isotherm experiments were performed at pH 5.0 ± 0.1 in solutions with initial adsorptive concentrations of 1–100 mg As^V L^{-1} (i.e., 1, 5, 10, 20, 40, 60, 80, and 100 mg L^{-1}) or 1–50 mg F^- L^{-1} (i.e., 1, 2, 5, 10, 20, 30, 40, and 50 mg L^{-1}) in the case of single adsorptive test. In the dual adsorptive test, the initial concentrations of As^V and F^- of the solution varied simultaneously following

the above set of intervals. The experiments were conducted with a constant solid-liquid ratio of adsorbent (2 g L^{-1}) at 10 °C and 30 °C, respectively. The data were fitted by Freundlich and Langmuir models in the form of Eqs. (1) and (2).

Freundlich model:

$$Q_e = K_F C_e^{1/n} \quad (1)$$

Langmuir model:

$$Q_e = \frac{K_L Q_m C_e}{1 + K_L C_e} \quad (2)$$

where Q_e (mg g^{-1}) is the adsorption capacity at equilibrium, C_e is the equilibrium As^V and F^- concentration in mg g^{-1}, n and K_F are the Freundlich constant; Q_m is the maximum adsorption capacity in mg g^{-1}, K_L is the Langmuir constant related to adsorption energy.

2.4. Recyclability test

MgAl-mBC and the pristine mBC were chosen for the recyclability test using the method specified elsewhere (Li et al., 2019). In brief, after equilibrating in an As^V+F^- mixture solution ([As^V] = [F^-] = 10 mg L^{-1}) on a Lab quake tube rotator for 24 h, the exhausted adsorbents were magnetically separated from the suspensions using an external magnet for 10 s (inset of Fig. 7A) and rinsed with 5 mL of dilute NaOH (0.1 M). Then, the obtained adsorbents were further rinsed with 20 mL of ultrapure water and magnetically separated from the rinsing water for the next adsorption cycle. The recyclability tests were performed at 25 °C for five successive cycles.

3. Results and discussions

3.1. Properties of magnetic biochars

Fig. 1A presents the XRD patterns of the mBCs and the pristine biochar (labeled as BC). The broad carbon peak over the 2θ range of 15–30° (orange curve) indicates that BC is mainly composed of amorphous carbon (Xiao et al., 2014). The XRD reflections of mBC (olive curve) at 2θ = 24.1°, 33.1°, 35.6°, 40.9°, 49.4°, 54.1, 57.5°, 62.4°, 63.9° and 71.9° are respectively attributed to the (012), (104), (110), (113), (024), (116), (122), (214), (300), and (1010) planes of hematite (JCPDS # 89–0596). The peaks at 2θ = 35.6°, 43.1°, 57.3°, and 62.8° are assignable to the (311), (400), (511) and (440) planes of maghemite (JCPDS # 39–1346), respectively. Besides, fayalite (JCPDS # 70–1861) was also evidenced by the peaks at 2θ = 25.2°, 31.7°, 37.3°, 51.5°, 61.1° and 62.3°, which can be attributed to the (111), (130), (222), (240), (062) and (321) planes, respectively. After anchoring of Al salt followed by pyrolysis, gibbsite (JCPDS # 33–0018) was observed for the Al-anchored magnetic biochar (Al-mBC, blue curve) besides hematite and maghemite. Unlike Al-mBC, Mg-anchored magnetic biochar (Mg-mBC, red curve) is featured with two different new phases, i.e., periclase (JCPDS # 75–0447) and wuestite (JCPDS # 85–0625) along with maghemite. Note that a wealth of reflections assignable to spinel (JCPDS # 75–0447) was evident for MgAl-mBC (black curve) aside from both wuestite and maghemite. No strong and sharp reflection attributed to carbon was found for all the mBCs, indicating that the biochar matrices are probably in the form of amorphous and/or poor crystallized (Zhang et al., 2013).

Fig. 1B shows the FT-IR spectra of the mBCs. The IR bands at 3400−3700 cm^{-1} and peaks at 1577−1625 cm^{-1} are derived from the O–H stretching and bending vibration of hydrogen-bonded OH groups, respectively (Jung et al., 2015). The bands at 2922 and 2850 cm^{-1} correspond to polymeric C–H groups (Venkateswarlu et al., 2016). The bands at 1399 and 1384 cm^{-1} are ascribable to polymeric –COO− stretching and phenolic O–H blending respectively, whereas the band at 1108 cm^{-1} is attributed to aromatic C–O groups (Venkateswarlu et al., 2016; Xiao et al., 2014). Besides, the aromatic C–H vibrations (deformation and/or bending) are also evident for the pristine mBC (bands at 815, 872, and 952 cm^{-1}) and Mg- and MgAl-mBC (695, 890, and 1005 cm^{-1}) (Keiluweit et al., 2010). The bands within 400–600 cm^{-1} including 535 and 470 cm^{-1} were generally attributed to lattice stretching vibrations of M−O (i.e., Fe–O, Al–O, and Mg–O) (Ji et al., 2017). These observations suggested that the magnetic biochar matrices are likely a blend of aromatic and aliphatic carbon in both amorphous and poor crystallized forms, which are derived from the pyrolysis process in the presence of metal salts (Xiao et al., 2014).

The specific surface areas and porosity of the mBCs were determined by the N_2 adsorption analysis at 77 K and the results are given in Fig. 1C and D. The N_2 adsorption and desorption isotherms of all mBCs can be classified as type II isotherms (IUPAC classification) with a hysteresis loop of type H3 at high relative pressures (0.45–1.0). This type of isotherm is indicative of mesopores derived from the stacking of flaky materials (Kaneko, 1994; Li et al., 2019). The specific surface areas of the pristine mBC, Al-mBC, Mg-mBC, and MgAl-mBC are 205, 116, 80, and 114 m^2 g^{-1}, respectively, as calculated using the Brunauer-Emmett-Teller (BET) model. Note that the pore size distribution data (Fig. 1D) of these samples were calculated by the Barrett-Joyner-Halenda (BJH) model using the adsorption isotherm data. The average pore sizes of all mBCs are in the range of mesopore (i.e., 2–50 nm), confirming the existence of mesopores in the materials.

SEM images in Fig. 2 display the morphology of the magnetic biochars. All the magnetic biochars are composed of irregular rubble-like particulate carbon. A good dispersion of small micro-sized crystals corresponding to iron oxides including fayalite, hematite, and maghemite had been partly embedded in the biochar matrix of the pristine mBC sample (Fig. 2A). This is indicative of good mechanical bonding between the biochar matrix and the iron oxide particles and enhanced stability of the magnetic biochar (Zhang et al., 2013). With the anchoring of either Al or Mg salts, the surfaces of these mBCs seem to become smoother than the pristine mBC (Fig. 2B−2D), leading to a gradual decrease in the specific surface areas of the mBCs as mentioned above. The smoothest magnetic biochar was found to be Mg-mBC (Fig. 2C) with the smallest specific surface area (i.e., 80 m^2 g^{-1}). This observation is in good agreement with the above N_2 adsorption analysis data.

3.2. Points of zero charge

The points of zero charge (PZC) values measured on a Zetasizer (Nano ZS 90, Malvern) in the presence of 1 mM $NaNO_3$ were 7.4, 6.5, 7.0, and 6.9 for mBC, Al-mBC, Mg-mBC, and MgAl-mBC, respectively (Fig. 3). These PZC data are comparable to those as reported in the literature, such as iron-anchored granular activated carbon (PZC = 7.3) (Dastgheib et al., 2004), and other metal-anchored biochars (PZC = 6.3–9.0) (Han et al., 2015; Jung et al., 2017). In the presence of 1 mM F^- ions along with 1 mM $NaNO_3$, the adsorption of F^-on these mBCs only produces small shifts (<0.6 pH unit) in the PZC (Fig. 3). However, the PZC values of mBC, Al-mBC, Mg-mBC, and MgAl-mBC have shifted apparently by −2.6, −1.7, −2.0, and −2.0 pH units as a result of As^V adsorption. Generally, a decrease in PZC values (i.e., PZC shifts) of a mineral as a result of adsorption reactions is macroscopic indicative of inner-sphere complexation of anion adsorbates caused by an increase in net surface charge (Goldberg, 2014). Considering that the mBCs are mixtures of organic and inorganic components (Fig. 1), it is thus unconvinced to deduce the actual adsorption mechanism simply by the PZC shifts. Nevertheless, the PZC shifts by the adsorption of As^V are greater than F^- adsorption, implying that As^V has a higher affinity towards the mBCs.

3.3. Adsorption envelops

The influence of ionic strength (***I***) and initial adsorptive concentration (C_0) at varying pH values on the adsorption of As^V and F^- on the

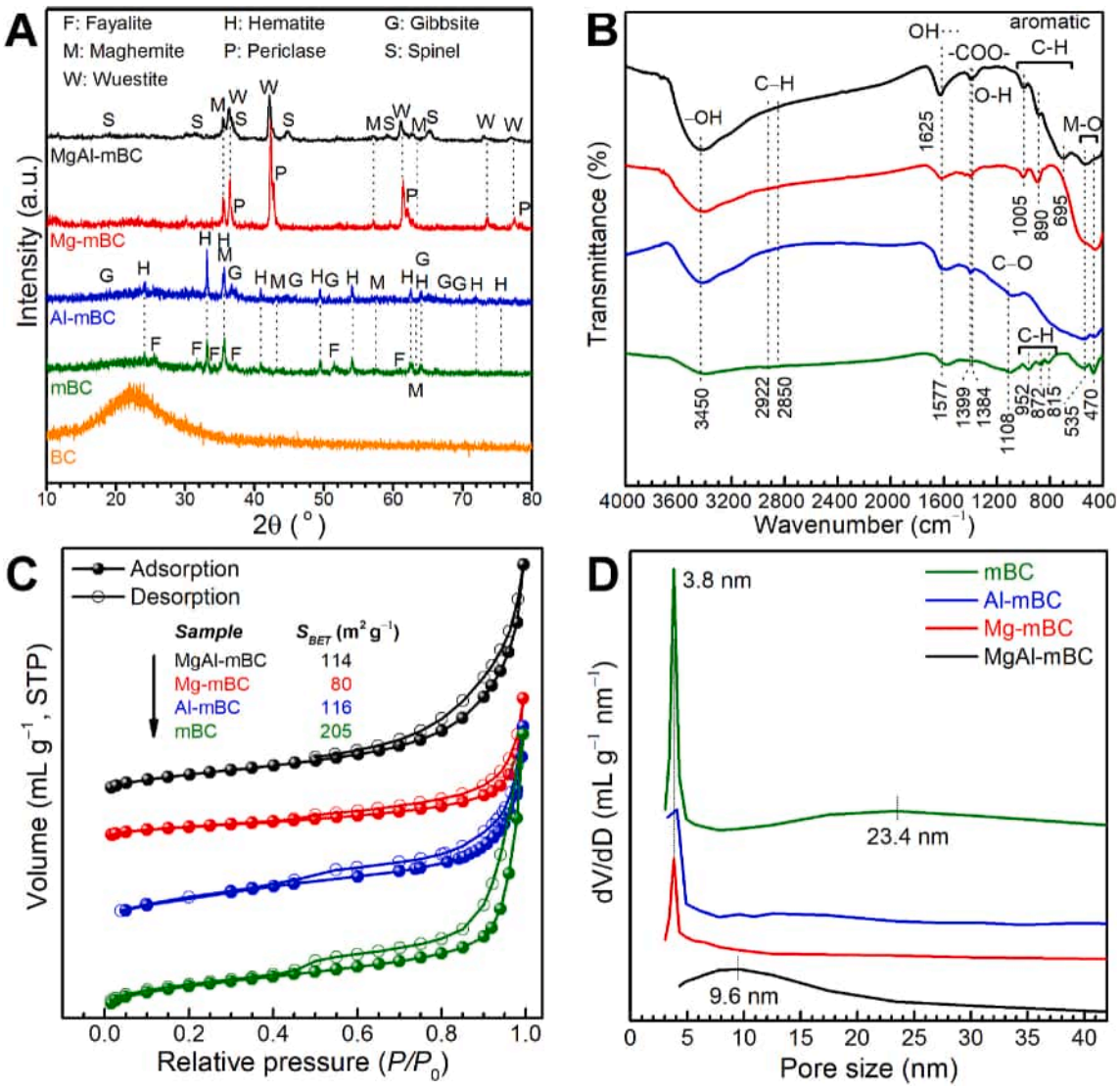

Fig. 1. Characterizations of the magnetic biochars. (A) XRD patterns; (B) FT-IR spectra; (C) N_2 adsorption-desorption isotherms; (D) the corresponding BJH pore size distribution graphs.

MgAl-mBC adsorbent are shown in Fig. 4. Besides the 'PZC shifts' method, ionic strength dependence is also widely used to distinguish between the inner-sphere and outer-sphere indirectly (Goldberg, 2014). Note that the As^V adsorption percentage of the MgAl-mBC at $C_0 = 10$ mg L^{-1} (ppm) decreases apparently and independently of ionic strength as pH increases from 4 to 11 (Fig. 4A). This behavior is indicative of the inner-sphere adsorption mechanism. Likewise, F^- adsorption also shows slight ionic strength dependence at pH > 7, indicating that F^- was likely to be sequestered via ligand exchange at pH > 7 (Li et al., 2019). At pH < 7, F^- adsorption is ionic strength dependent and negatively correlated with ionic strength (Fig. 4C). Ions showing considerable ionic strength dependence were believed to be weakly adsorbed as outer-sphere surface complexes (Goldberg, 2014). It is, therefore, reasonable to speculate that F^- ions were likely to link to the protonated metal hydroxyls (>M-OH_2^+) of the positively charged surface of the MgAl-mBC at pH < 7 (approximately equal to PZC of MgAl-mBC, see Fig. 3D) via the Coulomb attraction. Note that adsorption of both As^V and F^- on mBC exhibits marked ionic strength dependence (Fig. S1), implying that both anions were likely to form outer-sphere surface complexes. As^V adsorption on Mg-mBC and F^- adsorption on Al-mBC (Figs. S2, S3), conversely, show weak ionic strength dependence, suggesting the formation of strong surface complexes.

As shown in Fig. 4B, As^V adsorption is also highly dependent on the initial As^V concentration. The higher the initial As^V concentration over the range of 2–30 ppm, the lower the adsorption percentage. Similar trends have been observed in several earlier studies for As^V adsorption onto hydrous ferric oxide (HFO) and goethite (Dixit and Hering, 2003), and iron oxide impregnated activated carbon (FeAC) (Vaughan and Reed, 2005). However, the amount of F^- adsorbed on MgAl-mBC increases slightly with pH from 4 to 6, and then decreases gradually at pH 6–11 when the initial F^- concentrations (C_{0-F}) are 2 and 10 ppm, respectively (Fig. 4D). In the case of C_{0-F} = 30 ppm, F^- adsorption shows a similar trend as As^V. Note that the pH_{PZC} of MgAl-mBC was shifted from 6.9 to 6.4 in the presence of 1 mM F^- (i.e., 19 ppm) (see Fig. 3D). It can be expected that the pH_{PZC} would be greater than 6.4 in the presence of 10 ppm or less F^-. Therefore, when C_{0-F} is respectively 2 and 10 ppm, the surface of MgAl-mBC remains positively charged at pH 4–6, leading to a slight increase of F^- adsorption by the Coulomb attraction. When C_{0-F} is 30 ppm, the positively charged surface would be neutralized quickly by the excess F^-, and thus results in a decrease of F^- adsorption in the pH range of the experiments. Similar trends were also evident for As^V and F^- adsorption onto mBC, Al-mBC, and Mg-mBC (see Figs. S1-3, Supplementary data), implying similar adsorption mechanisms.

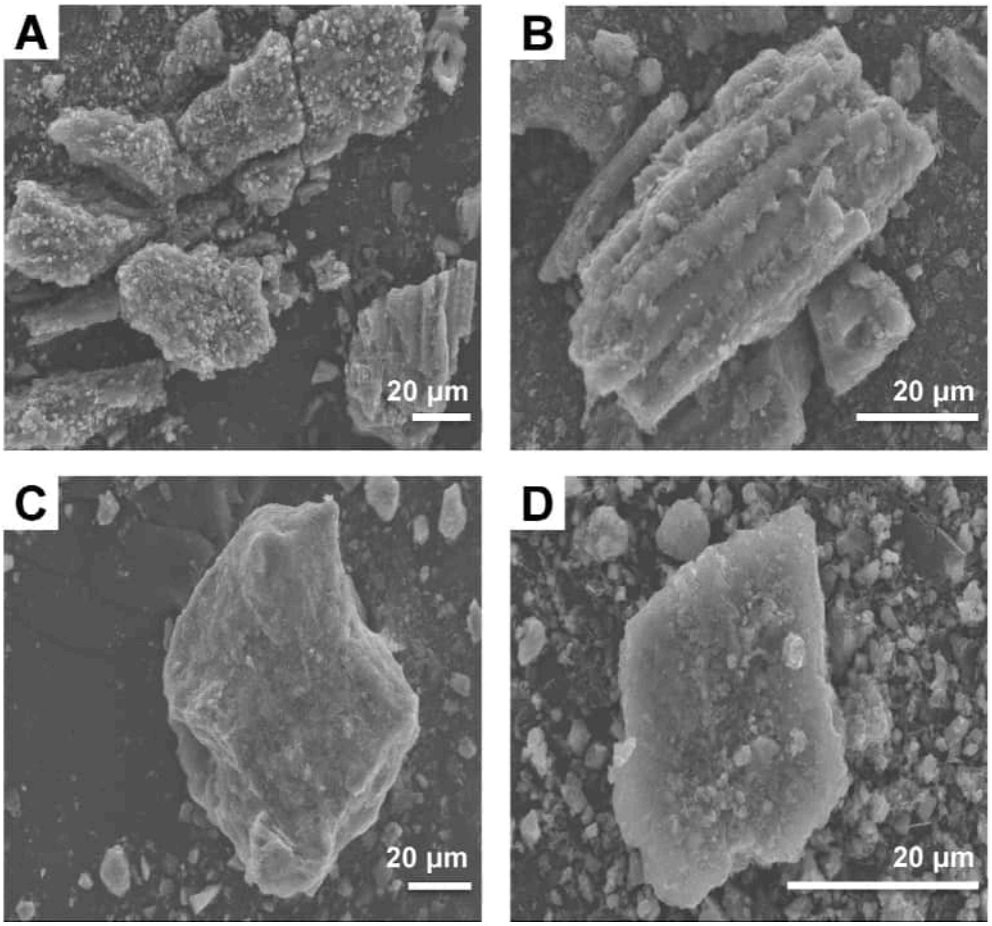

Fig. 2. SEM images of magnetic biochar: (A) mBC, (B) Al-mBC, (C) Mg-mBC, and (D) MgAl-mBC.

To assess the contribution of dissimilar surface functional groups of the mBCs to the adsorption, both the As^V and F^- adsorption under the same conditions (i.e., $C_0 = 2$ ppm, and $I = 10$ mM $NaNO_3$) are compared and the results are shown in Fig. 5. Quite clearly, the adsorption of either As^V or F^- has been improved to some extent compared to the pristine mBC due to the presence of surface metal hydroxyls, >M-OH (M = Mg, Al). Note that the maximum As^V adsorption onto all mBCs occurred at pH 4, and adsorption percentages follow the order of MgAl-mBC > Mg-mBC > Al-mBC > mBC in the pH range of 4–11 (Fig. 5A), indicating that > Mg–OH might have a greater affinity towards As^V than > Al–OH. The As^V adsorption percentages have been enhanced by 39.8, 27.1, and 19.8% for MgAl-mBC, Mg-mBC, and Al-mBC, respectively as compared to the pristine mBC. With respect to F^-, the maximum adsorption occurred at pH 5–6. The F^- adsorption percentage follows the order of MgAl-mBC > Al-mBC > Mg-mBC > mBC in the pH range of 4–6, whereas, in pH 6–11, it follows the order of Al-mBC > MgAl-mBC > Mg-mBC > mBC (Fig. 5B). This implies that F^- would prefer to adsorb to > Al–OH rather than > Mg–OH.

3.4. Adsorption isotherms

The adsorption isotherms of the target adsorbates (i.e., As^V and/or F^-) in solutions containing single and/or dual adsorptive (i.e., As^V and/or F^- in the bulk solution) on these mBCs are given in Fig. 6, S4 − S6. The isotherm data show a similar trend that the adsorption capacity (Q_e) of the adsorbent increases with the equilibrium concentration (C_e) in a near-exponential fashion. In other words, the slopes of the isotherms decrease with C_e since the vacant binding sites decrease as the adsorption proceeds. This behavior is a feature of the L-type isotherm, implying that the high affinity of the mBCs adsorbents for both adsorbates (i.e., As^V or F^-) at low concentrations, which then decreases as the concentration increases. The data could be fit using both the Freundlich and the Langmuir models (Eqn. (1) and (2)), and the corresponding fitted parameters with standard error (SE) and the correlation coefficients are tabulated in Table 1. Note that the SEs of these fitted parameters in the brackets are relatively small and that the correlation coefficients (R^2) of both models are high and comparable for all the metal-anchored mBC adsorbents, indicating that both models can well depict and predict the adsorption behaviors. In the case of the pristine mBC, it seems that the Langmuir model rather than the Freundlich model can well fit the adsorption isotherm data as indicated by the corresponding higher correlation coefficients (Table 1). Generally, the Langmuir model assumes a monolayer surface adsorption at specific homogeneous sites, whereas the Freundlich model presumes a multi-layer adsorption on the heterogeneous sites. Therefore, the adsorption of either As^V or F^- on these mBCs is likely to occur on both homogeneous and heterogeneous surface sites. It is also observed that the $1/n$ values derived from the Freundlich model range from 0.25 to 0.62 (Table 1), yielding n values in the range of 1.6–4.0, indicative of favorable adsorption for both anions (Lin et al., 2019b).

The influence of temperature (10, and 30 °C) was also considered in the adsorption isotherm experiments. Note that the effect of temperature on the maximum adsorption capacity (Q_m) of a specific mBC adsorbent varied randomly with either the adsorbate or the solution (Table 1). This implies that As^V and F^- adsorption onto the mBCs can be either endothermic or exothermic, in good agreement with previous reports (Deng et al., 2010; Li, 2013). In comparison to the pristine mBC, the maximum adsorption capacities (Q_m) of metal-anchored mBCs towards both As^V and F have been greatly improved due to the formation of surface metal hydroxyls, >M-OH (M = Mg, Al) via metal anchoring to the pristine

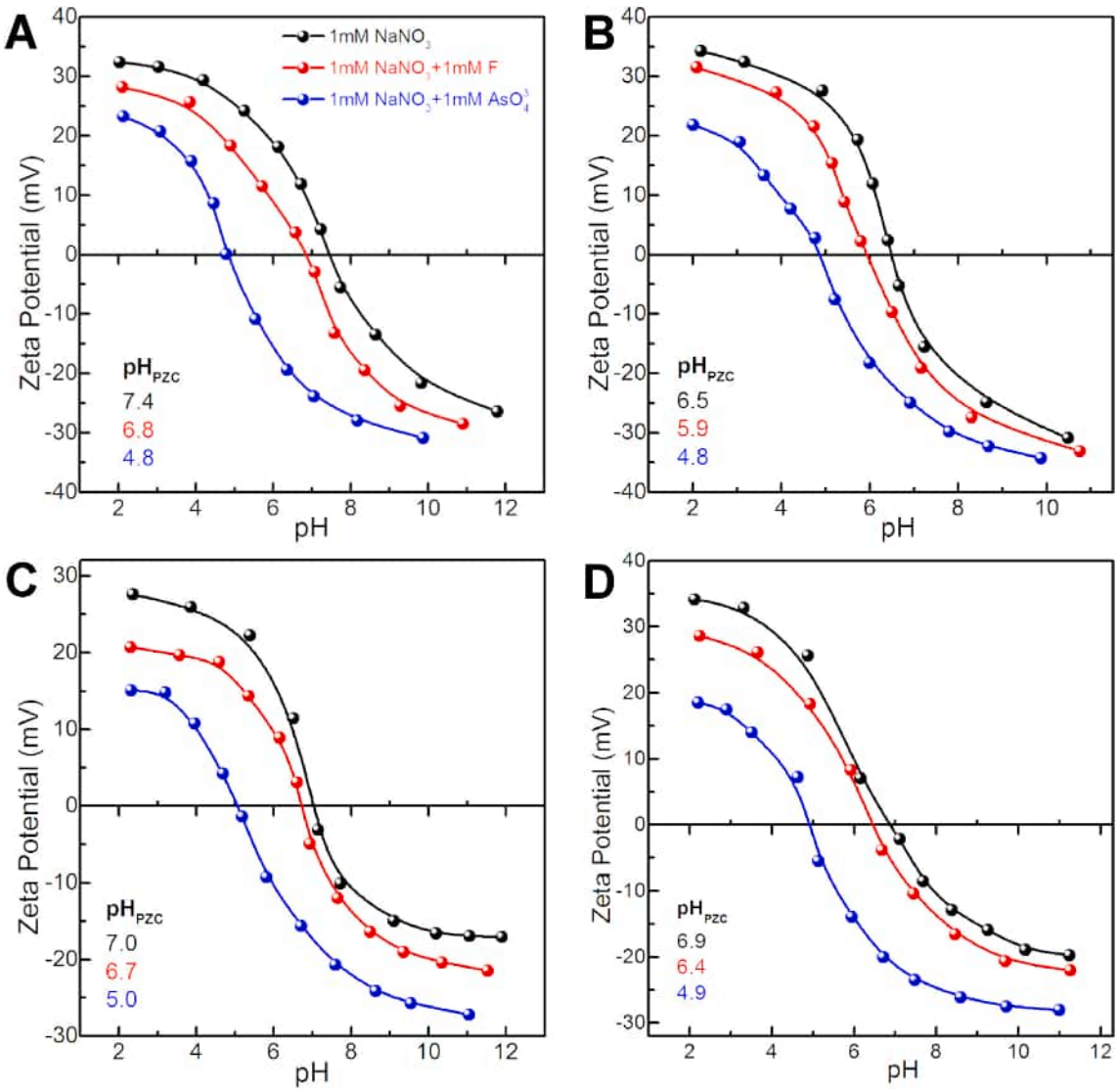

Fig. 3. Zeta (ζ) potential profiles of (A) mBC, (B) Al-mBC, (C) Mg-mBC, and (D) MgAl-mBC in the absence or presence of either arsenate or fluoride. (I = 1 mM $NaNO_3$, adsorbent dosage = 0.1 g L^{-1}, T = 25 °C).

mBC.

As shown in Table 1, the MgAl-mBC adsorbent exhibited the highest Q_m among all mBCs. The maximum As^V and F^- adsorption capacities ($Q_{m\text{-}As}$ and $Q_{m\text{-}F}$) of MgAl-mBC at 10 °C in solutions with single adsorptive are 34.45 and 21.59 mg g^{-1}, respectively. In the case of adsorption in solutions with dual adsorptive, however, the $Q_{m\text{-}As}$ and $Q_{m\text{-}F}$ of MgAl-mBC decreased respectively to 18.86 mg g^{-1} (a reduction of 45.2%), and 9.71 mg g^{-1} (a reduction of 55.0%). This implies that both As^V and F^- competed with each other for the binding sites, i.e., >M-OH (M = Mg, Al) during the adsorption process (Merodio-Morales et al., 2020). This competitive adsorption between As^V and F^- is also well-documented for other metal oxides (Li et al., 2019; Liu et al., 2012). Comparing the maximum adsorption capacities of all the metal-anchored mBCs with other biochars in the literature (Table 2) makes it clear that the metal-anchored mBCs outperform significantly other biochars and are promising for application in simultaneous removal of both As^V and F^- from wastewater.

3.5. Recycling performance

Recyclability and/or reusability is one of the most significant concerns for the potential of industrial-scale applications as well as the cost-effectiveness when designing a specific adsorbent. The magnetic property of adsorbents enables them to be fast and magnetically separated from the suspensions after adsorption (Zhang et al., 2013). Fig. 7 shows the recyclability results of both mBC and MgAl-mBC adsorbents. The adsorption percentages of either As^V or F^- decreased with the recycling cycle in a near-linear fashion. The As^V adsorption percentages of mBC and MgAl-mBC, for instance, have decreased respectively from 44.0, to 63.2% to 18.8, and 32.5% after successive five recycling cycles (Fig. 7A). Likewise, the F^- adsorption percentages of mBC and MgAl-mBC have reduced by 54.8, and 44.4%, respectively (Fig. 7B). The recyclability recession of both adsorbents is probably on account of the loss of surface metal hydroxyls, >M-OH (M = Mg, Al, and Fe), during the rinsing process using dilute NaOH. Nevertheless, it is worth noting that both adsorbents possess good magnetic properties, allowing them to be fast and easily recovered by an external magnet in approximately 10 s (inset of Fig. 7A). Additionally, the rinsing process with dilute NaOH and ultrapure water can be done in less than 2 min, making the recycling process highly efficient. The high recycling performance and the high adsorption efficiency are convinced that the MgAl-mBC adsorbent has a good potential for large-scale applications in As^V and F^--polluted wastewater remediation.

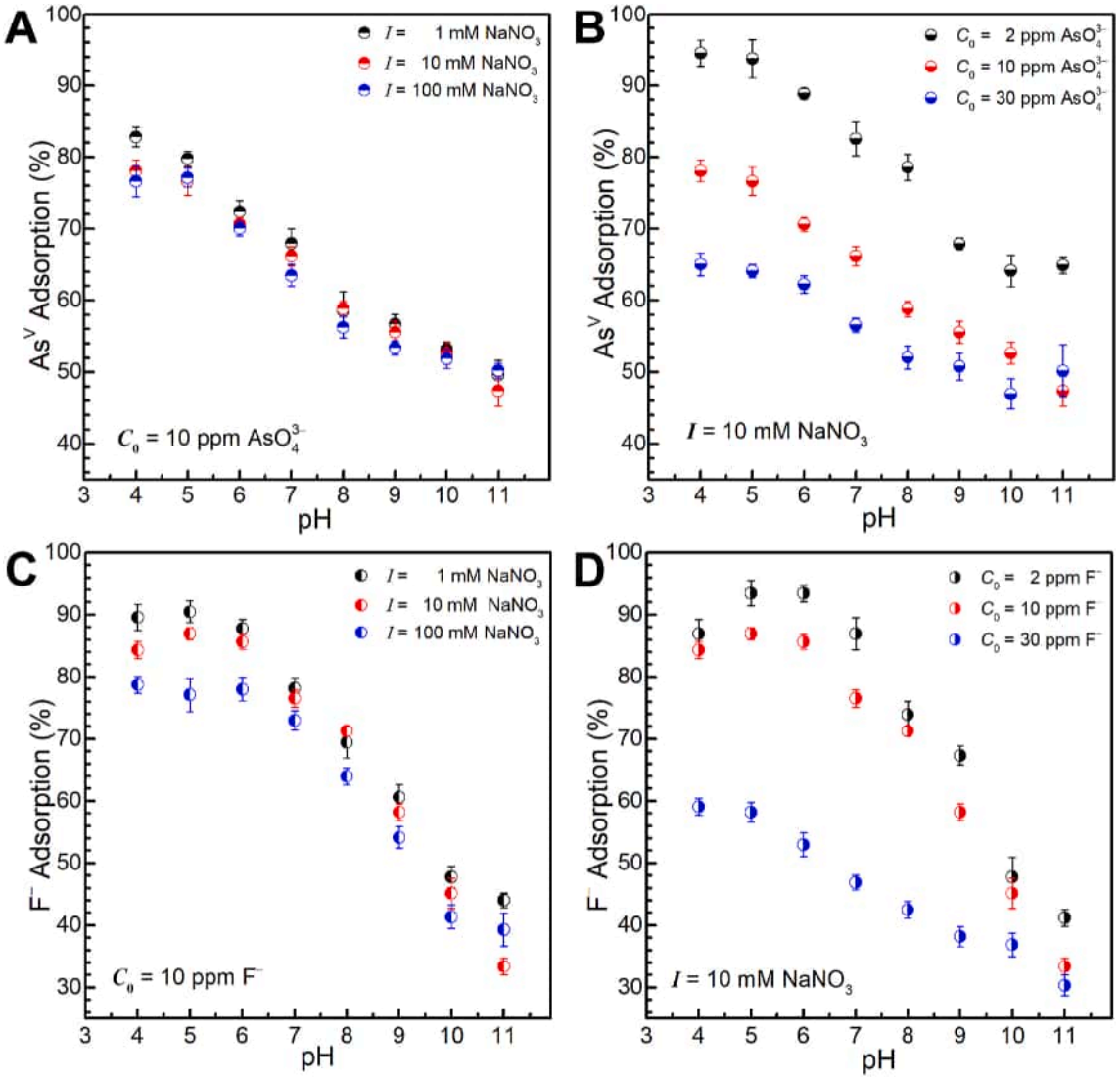

Fig. 4. Arsenate (A, B) and fluoride adsorption curves (C, D) on MgAl-mBC as a function of pH, ionic strength (I), and initial adsorptive concentration (C_0).

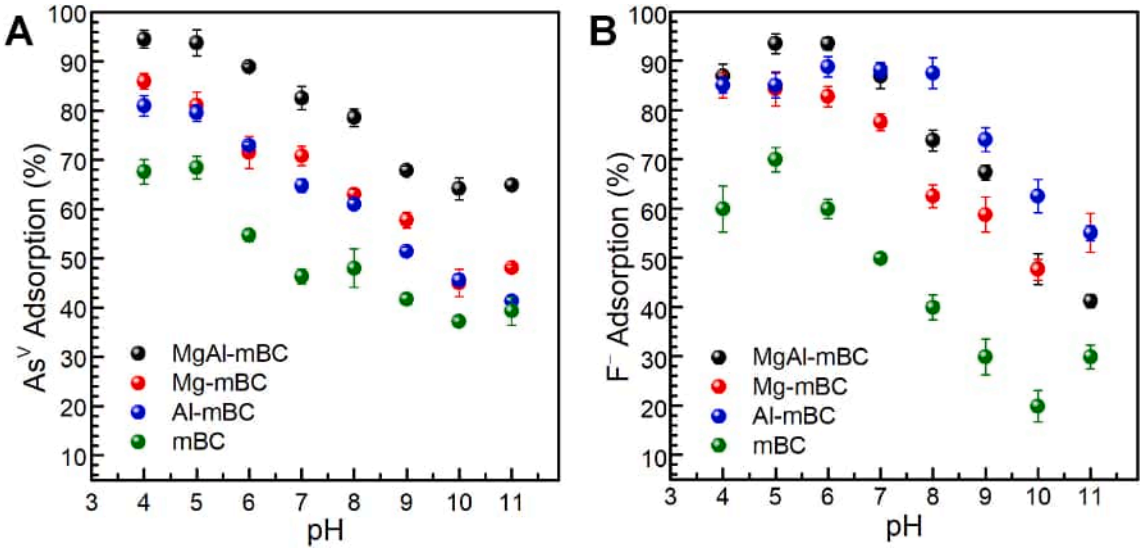

Fig. 5. Comparison of arsenate (A) and fluoride (B) adsorption onto mBC, Al-mBC, Mg-mBC, and MgAl-mBC at $C_0 = 2$ ppm, and $I = 10$ mM $NaNO_3$. Data are taken from Fig. 4 and S1−3.

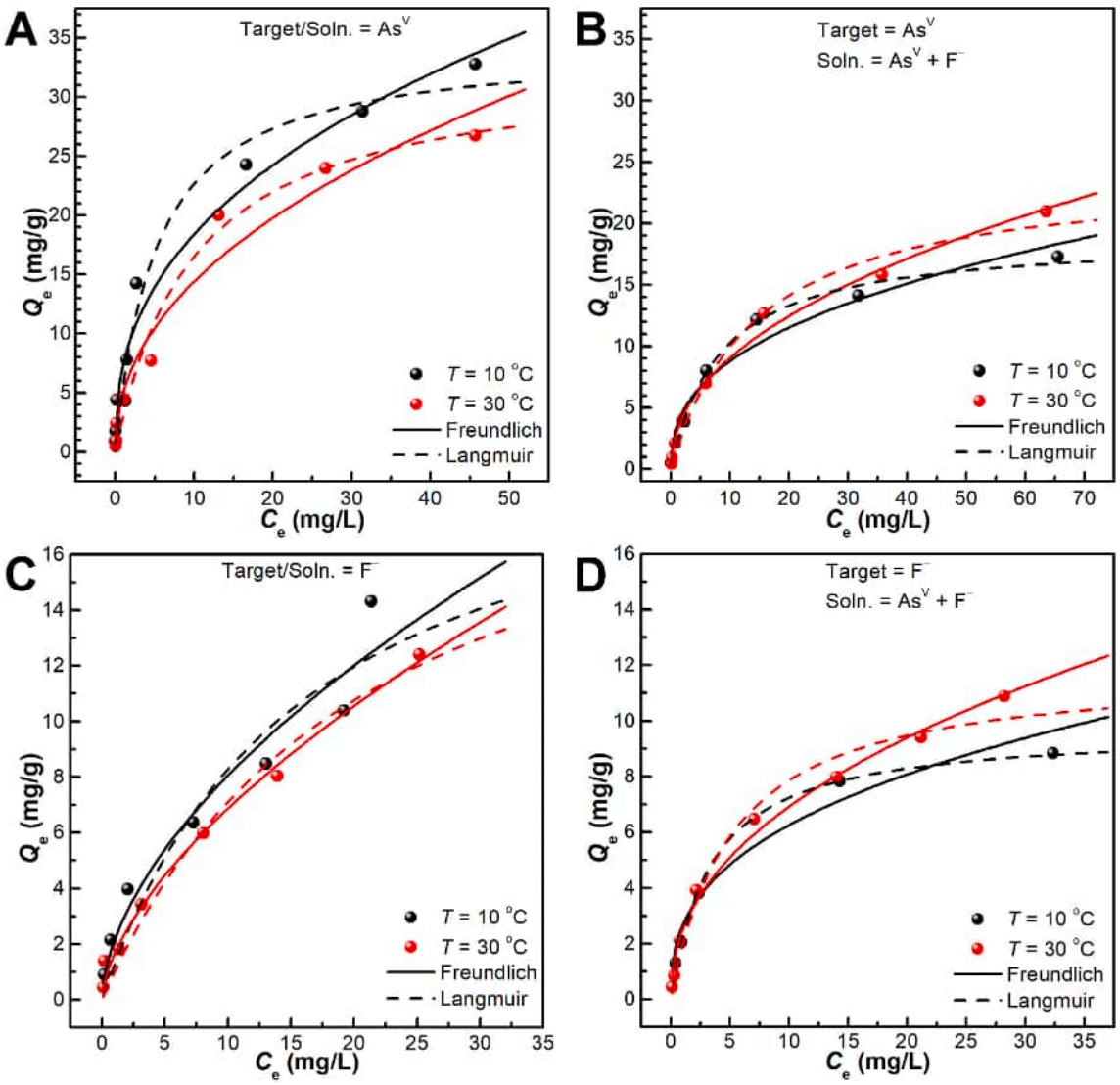

Fig. 6. Adsorption isotherms of As^V and F^- on MgAl-mBC in solutions containing single (A, C) and/or duel (B, D) adsorptive at pH = 5.0 ± 0.1.

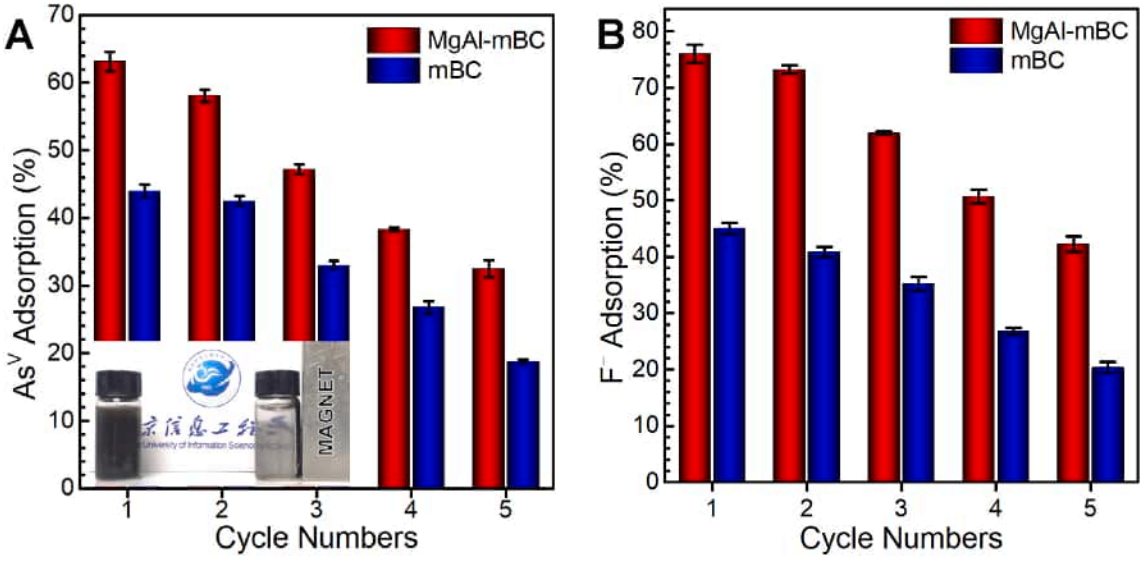

Fig. 7. Recycling performance of the mBC and MgAl-mBC adsorbents for adsorption of (A) arsenate and (B) fluoride in successive five cycles.

Table 1
Langmuir and Freundlich fitted parameters with standard error (SE) for As^V and F^- adsorption onto the mBCs.

Adsorbent	Target adsorbate	Solution	T (°C)	Freundlich			Langmuir		
				K_F	$1/n$	R^2	Q_m (mg g^{-1})	b (L mg^{-1})	R^2
mBC	As^V	As^V	10	1.57 (0.29)	0.26 (0.05)	0.860	4.59 (0.16)	0.36 (0.06)	0.979
			30	1.19 (0.26)	0.30 (0.06)	0.865	4.32 (0.26)	0.20 (0.05)	0.954
	F^-	F^-	10	1.23 (0.24)	0.34 (0.06)	0.890	4.28 (0.26)	0.27 (0.07)	0.958
			30	0.95 (0.18)	0.41 (0.06)	0.936	4.76 (0.36)	0.14 (0.04)	0.963
	As^V	$As^V + F^-$	10	1.00 (0.22)	0.28 (0.06)	0.840	3.36 (0.34)	0.22 (0.1)	0.863
			30	1.21 (0.23)	0.25 (0.05)	0.852	3.46 (0.13)	0.37 (0.07)	0.971
	F^-	$As^V + F^-$	10	0.90 (0.16)	0.27 (0.05)	0.852	2.35 (0.15)	0.52 (0.18)	0.905
			30	0.78 (0.13)	0.30 (0.05)	0.892	2.37 (0.12)	0.33 (0.07)	0.965
Al-mBC	As^V	As^V	10	2.16 (0.32)	0.44 (0.04)	0.975	15.75 (0.89)	0.07 (0.01)	0.987
			30	2.19 (0.42)	0.45 (0.05)	0.959	16.45 (1.19)	0.07 (0.01)	0.981
	F^-	F^-	10	2.53 (0.29)	0.47 (0.04)	0.982	14.64 (1.15)	0.12 (0.03)	0.984
			30	3.54 (0.50)	0.42 (0.05)	0.954	14.55 (0.58)	0.25 (0.03)	0.992
	As^V	$As^V + F^-$	10	2.17 (0.43)	0.35 (0.05)	0.922	9.52 (0.72)	0.17 (0.05)	0.949
			30	2.21 (0.47)	0.30 (0.06)	0.871	7.81 (0.29)	0.24 (0.04)	0.984
	F^-	$As^V + F^-$	10	3.47 (0.65)	0.42 (0.07)	0.922	14.70 (0.99)	0.24 (0.05)	0.978
			30	2.62 (0.06)	0.54 (0.01)	0.999	19.41 (1.88)	0.10 (0.02)	0.986
Mg-mBC	As^V	As^V	10	2.76 (0.44)	0.41 (0.04)	0.965	16.66 (0.95)	0.09 (0.01)	0.986
			30	2.47 (0.50)	0.46 (0.05)	0.958	20.27 (2.61)	0.06 (0.02)	0.958
	F^-	F^-	10	2.48 (0.25)	0.48 (0.03)	0.987	14.38 (2.08)	0.13 (0.05)	0.950
			30	1.43 (0.15)	0.57 (0.04)	0.991	13.03 (1.87)	0.08 (0.02)	0.978
	As^V	$As^V + F^-$	10	2.92 (0.69)	0.33 (0.06)	0.870	11.30 (0.39)	0.22 (0.03)	0.989
			30	2.87 (0.64)	0.36 (0.06)	0.907	13.41 (0.50)	0.15 (0.02)	0.990
	F^-	$As^V + F^-$	10	2.15 (0.24)	0.54 (0.04)	0.987	17.02 (1.13)	0.09 (0.01)	0.993
			30	3.66 (0.80)	0.34 (0.07)	0.849	11.43 (1.04)	0.39 (0.13)	0.928
MgAl-mBC	As^V	As^V	10	7.34 (0.90)	0.40 (0.04)	0.972	34.45 (2.16)	0.19 (0.04)	0.970
			30	5.01 (0.79)	0.46 (0.05)	0.966	32.87 (2.66)	0.10 (0.02)	0.977
	F^-	F^-	10	2.14 (0.53)	0.58 (0.09)	0.953	21.59 (7.70)	0.06 (0.04)	0.919
			30	1.65 (0.18)	0.62 (0.04)	0.990	22.11 (4.82)	0.05 (0.02)	0.970
	As^V	$As^V + F^-$	10	3.57 (0.55)	0.39 (0.04)	0.963	18.86 (0.68)	0.12 (0.01)	0.993
			30	3.14 (0.31)	0.46 (0.03)	0.990	24.30 (1.83)	0.07 (0.01)	0.982
	F^-	$As^V + F^-$	10	2.67 (0.38)	0.37 (0.05)	0.943	9.71 (0.20)	0.29 (0.02)	0.997
			30	2.50 (0.21)	0.44 (0.03)	0.989	11.92 (0.78)	0.19 (0.04)	0.980

Table 2
Comparison of the maximum adsorption capacities of mBCs with other biochars reported previously in the literature.

Adsorbent	Experimental conditions	Q_m (mg g^{-1})		Ref.
		As^V	F^-	
Magnetic corn stover biochar	pH = 2.0, T = 25 °C	–	4.11	Mohan et al. (2014a)
Ni/Mn-LDH/ Biochar	pH = 8.0, T = 22 °C	6.52	–	Wang et al. (2016)
Perennial grass biochar	pH = 7.0, T = 26 °C	8.67	1.25	Saikia et al. (2017)
Yak dung biochar	pH = 5.0–6.0, T = 25 °C	3.93	2.93	Luo et al. (2018)
Fe–Mn–La loaded biochar	pH = 4.0–7.0, T = 25 °C	14.9	–	Lin et al. (2019a)
Bone char	–	0.056	2.33	Alkurdi et al. (2020)
La-loaded char	pH = 7, T = 30 °C	26.37	2.42	Merodio-Morales et al. (2020)
Al-mBC	pH = 5, T = 10 °C	15.75	14.64	This work
Mg-mBC	pH = 5, T = 10 °C	16.66	14.38	This work
MgAl-mBC	pH = 5, T = 10 °C	34.45	21.59	This work

3.6. Adsorption mechanism

As the Schindler diagram can provide useful insight into the differences between the Coulomb attraction (outer-sphere complexation) and the inner-sphere complexation, it has been adopted here to clarify the adsorption mechanisms (Fig. 8A, and B). The *pKa* of HF is approximately 3.17, and the relevant PCZ of the mBCs adsorbents vary from 6.5 to 7.4. Therefore, the Schindler diagram is featured by bottom bands with a set of horizontal lines (indicating the pH range of Coulomb attraction) from pH 3.17 to PZC (e.g., 6.5, 6.9, 7.0, and 7.4). The adsorption reactions between F^- and the mBCs adsorbents were observed to be very strong in the pH range of Coulomb attraction and decreased in a nearly linear fashion at pH > PZC due to the competition from the increasing OH^- in solution (Fig. 4C, and D, and Figs. S1-S3 C, and D) despite a weak attractive van der Waals force between F^- and the porous mBCs (Fulazzaky, 2011), implying that the Coulomb attraction mechanism dominates at pH < PZC and other reactions, such as ligand exchange or halogenation reaction probably predominate at pH > PZC. Likewise, As^V adsorption on these mBCs exhibits similar trends as F^- (Fig. 4A, and B and Figs. S1-S3 A, and B). For instance, in the presence of As^V (*pKa* = 2.19, 6.94, and 11.53), the surface of MgAl-mBC is positively charged at pH < 4.9 (Fig. 3D), and the dominant As^V species is $H_2AsO_4^-$ and $H_3AsO_4^0$. The Coulomb attraction between > M-OH_2^+ of the positively charged surface and $H_2AsO_4^-$ contributes significantly to the sequestration of As^V. As the solution pH rose to 5–11, the MgAl-mBC surface became negatively charged, and As^V species was predominated by $HAsO_4^{2-}$. Therefore, the Coulomb repulsion between the deprotonated surface metal hydroxyls (>M-O^-) of the negatively charged surface and $HAsO_4^{2-}$ will no doubt adversely affect As^V adsorption. Note that the inner-sphere complexation between the surface metal hydroxyls (>M-OH) and $HAsO_4^{2-}$ may remain in place, leading to a gradual rather than a sharp decline in As^V adsorption percentage (Fig. 4A, and B, and Figs. S1-S3 A, and B). This indicates that both Coulomb attraction and inner-sphere complexation mechanism are involved in the adsorption of As^V on the mBCs.

FT-IR spectra were adopted to interpret the adsorption mechanism. Fig. 8C shows the FT-IR spectra of the MgAl-mBC adsorbent before and after the adsorption of As^V and F^-. F^- adsorption onto the MgAl-mBC has led to a decrease in bands at 1005, and 890 cm^{-1}, and the disappearance of bands at 695, and 535 cm^{-1}, indicating that the aromatic C–H groups and the surface metal hydroxyls (>M-OH) were involved in F^- adsorption probably via halogenation and/or ligand exchange (Langlois et al., 1996). Likewise, the band at 535 cm^{-1} was lost and two new weak bands at 751, and 830 cm^{-1} ascribable to As–O vibration via Coulomb attraction and inner-sphere complexation, respectively

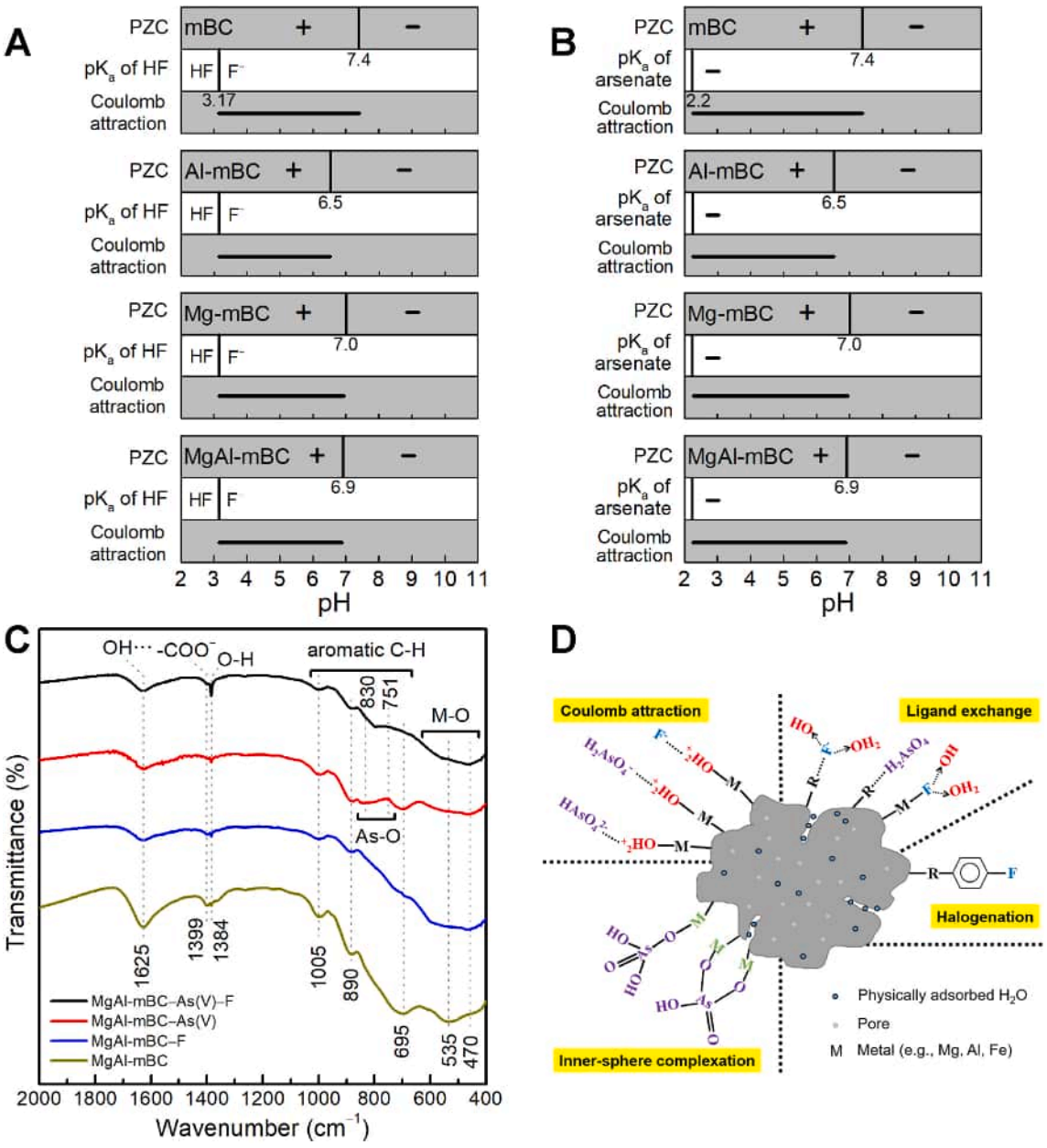

Fig. 8. Schindler diagram for (A) F^-, and (B) As^V adsorbing onto the mBCs adsorbents; (C) FT-IR spectra of MgAl-mBC before and after the adsorption of As^V and F^-; (D) the proposed adsorption mechanisms.

(Castaldi et al., 2010) were arisen after As^V adsorption, indicating that the surface metal hydroxyls (>M-OH) were probably associated with A^V adsorption. Note that the intensity of the band at 1399 cm^{-1} (polymeric –COO− group) has decreased after As^V adsorption. This was possibly due to the exchange between the carboxyl groups on the mBC surface and the As^V anions in the bulk solution (Lin et al., 2019a).

Another consideration in addition to the adsorption by the surface metal hydroxyls (>M-OH), is the uptake by the organic functional groups, including aromatic C–H, and polymeric –COO− groups as evidenced by the above FT-IR spectra interpretations (Fig. 8C). Therefore, the proposed adsorption mechanisms for As^V and F^- can be categorized into i) Coulomb attraction (Eqn. (3) – (4)); ii) inner-sphere complexation (Eqns. (5) and (6)); iii) ligand exchange (Eqns. (7)–(9)); and possibly iv) halogenation (Eqn. (10)) as illustrated in Fig. 8D and formularized as follows.

i) Coulomb attraction (outer-sphere complexation):

$$> MOH2 + +H2A_sO4 - \leftrightarrow > MOH2 + H2A_sO4- \quad (3)$$

$$> MOH2 + +F - \leftrightarrow > MOH2 + F- \quad (4)$$

ii) inner-sphere complexation:

$$>MOH_2^+ + H_2AsO_4^- \leftrightarrow >(MO)AsO(OH)_2 + H_2O \quad (5)$$

$$2>MOH_2^+ + H_2AsO_4^- \leftrightarrow >(MO)_2AsO(OH) + H^+ + 2H_2O \quad (6)$$

iii) ligand exchange:

$$>R–COO^- + H^+ + H_2AsO_4^- \leftrightarrow >R–H_2AsO_4 + HCOO^- \quad (7)$$

$$>R–COO^- + H^+ + F^- \leftrightarrow >R–F + HCOO^- \quad (8)$$

$$>MOH + F^- \leftrightarrow >M\text{-}F + OH^- \quad (9)$$

iv) halogenation:

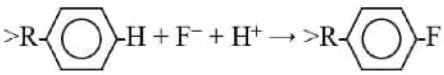

(10)

4. Conclusions

Magnetic biochars (mBCs) anchored with aluminum (Al) and/or magnesium (Mg) have been prepared via a facile pyrolysis method. It was observed that the adsorptions of either As^V or F^- on these mBCs are pH-dependent, and that both As^V and F^- are competing with each other for the surface binding sites of the mBCs, which led to a relatively lower adsorption efficiency in the dual adsorptive (As^V + F^-) systems as compared to that of the single adsorption (As^V or F^-) ones. Both the Langmuir and the Freundlich models can well describe the adsorption isotherm data in light of the relatively high correlation coefficients. The MgAl-mBC shows the highest adsorption capacities for both As^V and F^- for single adsorptive tests, i.e., 34.45 mg As^V g^{-1} (pH = 5, T = 10 °C), and 22.11 mg F^- g^{-1} (pH = 5, T = 30 °C), respectively. In the case of dual adsorptive systems, the Al-mBC displays the highest adsorption capacity for F^- (i.e., 19.41 mg F^- g^{-1} at pH = 5, T = 30 °C), while the MgAl-mBC outstrips other mBCs in As^V adsorption, showing an adsorption capacity as high as 24.30 mg As^V g^{-1} (pH = 5, T = 30 °C). Nevertheless, these mBCs exhibit much higher adsorption capacities for both As^V and F^- than other biochars reported in the literature under ambient conditions. Besides, the mBCs adsorbents can be fast reclaimed by magnetic separation and regeneration with dilute sodium hydroxide, allowing them to be used as alternative adsorbents for enhanced simultaneous removal of both As^V and fluoride from aqueous solution. Further work for environmental remediation may include the utilization of these mBCs adsorbents in bench-scale bed reactors for simultaneous removal of arsenate and fluoride from natural water matrices, and optimization of reaction and operational parameters, such as co-occurring competing ions, dissolved organic matters (DOMs), flow rate, and temperature, etc.

Credit author statement

Ziyi Shen: Conceptualization, Writing – original draft. Jie Jin: Writing – original draft, Visualization. Jingjing Fu: Methodology, Writing – original draft. Meng Yang: Funding acquisition. Feihu Li: Supervision, Funding acquisition, Writing – review & editing.

Declaration of competing interest

The authors declare that they have no known competing financial interests or personal relationships that could have appeared to influence the work reported in this paper.

Acknowledgments

The work was partially supported by the NUIST-UoR International Research Institute Research Fund, the National Natural Science Foundation of China (51002080, 41501197), Top-notch Academic Programs Project of Jiangsu Higher Education Institutions (PPZY2015C222), and the Priority Academic Program Development of Jiangsu Higher Education Institutions (PAPD).

Appendix A. Supplementary data

Supplementary data to this article can be found online at https://doi.org/10.1016/j.jenvman.2021.112898.

Nomenclature

AFS	atomic fluorescence spectroscopy
Al	aluminum
As	arsenic
As^V	arsenate
BC	the pristine biochar
BET	Brunauer-Emmett-Teller
BJH	Barrett-Joyner-Halenda
C_0	the initial adsorptive concentration
C_e	the equilibrium concentration
DOMs	dissolved organic matters
F	fluorine
F^-	fluoride
FeAC	iron oxide impregnated activated carbon
FT-IR	fourier Transform Infrared Spectroscopy
HFO	hydrous ferric oxide
I	ionic strength
JCPDS	Joint Committee Powder Diffraction Standards
Mg	magnesium
mBC	magnetic biochar
MCL	maximum contaminant level
PZC	the points of zero charge
Q_e	the adsorption capacity
Q_m	the maximum adsorption capacity
RPM	revolutions per minute
SE	standard error
SEM	scanning electron micrography
TLAC	titanium and lanthanum oxides anchored granular activated carbon
WHO	World Health Organization
XRD	X-ray diffraction

References

Ahmad, M., Rajapaksha, A.U., Lim, J.E., Zhang, M., Bolan, N., Mohan, D., et al., 2014. Biochar as a sorbent for contaminant management in soil and water: a review. Chemosphere 99, 19–33.

Alkurdi, S.S.A., Al-Juboori, R.A., Bundschuh, J., Bowtell, L., McKnight, S., 2020. Effect of pyrolysis conditions on bone char characterization and its ability for arsenic and fluoride removal. Environ. Pollut. 262, 114221.

Beg, S.A., Siddiqi, R.H., Ilias, S., 1982. Inhibition of nitrification by arsenic, chromium, and fluoride. J. Water Pollut. Control Fed. 54, 482–488.

Bibi, S., Farooqi, A., Hussain, K., Haider, N., 2015. Evaluation of industrial based adsorbents for simultaneous removal of arsenic and fluoride from drinking water. J. Clean. Prod. 87, 882–896.

Bibi, S., Kamran, M.A., Sultana, J., Farooqi, A., 2017. Occurrence and methods to remove arsenic and fluoride contamination in water. Environ. Chem. Lett. 15, 125–149.

Castaldi, P., Silvetti, M., Enzo, S., Melis, P., 2010. Study of sorption processes and FT-IR analysis of arsenate sorbed onto red muds (a bauxite ore processing waste). J. Hazard Mater. 175, 172–178.

Cuong, D.V., Wu, P.C., Chen, L.I., Hou, C.H., 2021. Active MnO2/biochar composite for efficient As(III) removal: insight into the mechanisms of redox transformation and adsorption. Water Res. 188, 116495.

Dastgheib, S.A., Karanfil, T., Cheng, W., 2004. Tailoring activated carbons for enhanced removal of natural organic matter from natural waters. Carbon 42, 547–557.

Daughney, C.J., Fakih, M., Chatellier, X., 2011. Progressive sorption and oxidation/hydrolysis of Fe(II) affects cadmium immobilization by bacteria-iron oxide composites. Geomicrobiol. J. 28, 11–22.

Deng, S.B., Li, Z.J., Huang, J., Yu, G., 2010. Preparation, characterization and application of a Ce-Ti oxide adsorbent for enhanced removal of arsenate from water. J. Hazard Mater. 179, 1014–1021.

Dixit, S., Hering, J.G., 2003. Comparison of arsenic(V) and arsenic(III) sorption onto iron oxide minerals: implications for arsenic mobility. Environ. Sci. Technol. 37, 4182–4189.

Fulazzaky, M.A., 2011. Determining the resistance of mass transfer for adsorption of the surfactants onto granular activated carbons from hydrodynamic column. Chem. Eng. J. 166, 832–840.

Goldberg, S., 2014. Application of surface complexation models to anion adsorption by natural materials. Environ. Toxicol. Chem. 33, 2172–2180.

Haldar, D., Duarah, P., Purkait, M.K., 2020. MOFs for the treatment of arsenic, fluoride and iron contaminated drinking water: a review. Chemosphere 251, 126388.

Han, Z.T., Sani, B., Mrozik, W., Obst, M., Beckingham, B., Karapanagioti, H.K., et al., 2015. Magnetite impregnation effects on the sorbent properties of activated carbons and biochars. Water Res. 70, 394–403.

Hu, X., Ding, Z.H., Zimmerman, A.R., Wang, S.S., Gao, B., 2015. Batch and column sorption of arsenic onto iron-impregnated biochar synthesized through hydrolysis. Water Res. 68, 206–216.

Inyang, M.I., Gao, B., Yao, Y., Xue, Y.W., Zimmerman, A., Mosa, A., et al., 2016. A review of biochar as a low-cost adsorbent for aqueous heavy metal removal. Crit. Rev. Environ. Sci. Technol. 46, 406–433.
Jadhav, S.V., Bringas, E., Yadav, G.D., Rathod, V.K., Ortiz, I., Marathe, K.V., 2015. Arsenic and fluoride contaminated groundwaters: a review of current technologies for contaminants removal. J. Environ. Manag. 162, 306–325.
Ji, H.S., Wu, W.H., Li, F.H., Yu, X.X., Fu, J.J., Jia, L.Y., 2017. Enhanced adsorption of bromate from aqueous solutions on ordered mesoporous Mg-Al layered double hydroxides (LDHs). J. Hazard Mater. 334, 212–222.
Jing, C.Y., Cui, J.L., Huang, Y.Y., Li, A.G., 2012. Fabrication, characterization, and application of a composite adsorbent for simultaneous removal of arsenic and fluoride. ACS Appl. Mater. Interfaces 4, 714–720.
Jung, K.W., Jeong, T.U., Hwang, M.J., Kim, K., Ahn, K.H., 2015. Phosphate adsorption ability of biochar/Mg-Al assembled nanocomposites prepared by aluminum-electrode based electro-assisted modification method with MgCl2 as electrolyte. Bioresour. Technol. 198, 603–610.
Jung, K.W., Lee, S., Lee, Y.J., 2017. Synthesis of novel magnesium ferrite (MgFe2O4)/biochar magnetic composites and its adsorption behavior for phosphate in aqueous solutions. Bioresour. Technol. 245, 751–759.
Kaneko, K., 1994. Determination of pore-size and pore-size distribution .1. Adsorbents and catalysts. J. Membr. Sci. 96, 59–89.
Keiluweit, M., Nico, P.S., Johnson, M.G., Kleber, M., 2010. Dynamic molecular structure of plant biomass-derived black carbon (biochar). Environ. Sci. Technol. 44, 1247–1253.
Koh, K.Y., Yang, Y., Chen, J.P., 2021. Critical review on lanthanum-based materials used for water purification through adsorption of inorganic contaminants. Crit. Rev. Environ. Sci. Technol. 51. https://doi.org/10.1080/10643389.2020.1864958.
Kumar, M., Goswami, R., Patel, A.K., Srivastava, M., Das, N., 2020. Scenario, perspectives and mechanism of arsenic and fluoride Co-occurrence in the groundwater: a review. Chemosphere 249, 126126.
Langlois, B., Gilbert, L., Forat, G., 1996. Fluorination of aromatic compounds by halogen exchange with fluoride anions ("halex" reaction). In: Desmurs, J.-R., Ratton, S. (Eds.), Industrial Chemistry Library. 8. Elsevier, pp. 244–292.
Li, F.H., 2013. Layer-by-layer loading iron onto mesoporous silica surfaces: synthesis, characterization and application for As(V) removal. Microporous Mesoporous Mater. 171, 139–146.
Li, F.H., Fu, J.J., Jin, J., Wang, S.L., Liu, Y.Y., Yang, M., et al., 2019. Evaporation-induced self-assembly (EISA) synthesized mesoporous bimetallic oxides (MBOs) enabling enhanced co-uptake of arsenate and fluoride from water. J. Chem. Technol. Biotechnol. 94, 879–891.
Li, W., Chen, D.H., Xia, F., Tan, J.Z.Y., Huang, P.P., Song, W.G., et al., 2016. Extremely high arsenic removal capacity for mesoporous aluminium magnesium oxide composites. Environmental Science-Nano 3, 94–106.
Lin, L.N., Song, Z.G., Khan, Z.H., Liu, X.W., Qiu, W.W., 2019a. Enhanced As(III) removal from aqueous solution by Fe-Mn-La-impregnated biochar composites. Sci. Total Environ. 686, 1185–1193.
Lin, L.N., Zhang, G.G., Liu, X.W., Khan, Z.H., Qiu, W.W., Song, Z.G., 2019b. Synthesis and adsorption of Fe-Mn-La-impregnated biochar composite as an adsorbent for As (III) removal from aqueous solutions. Environ. Pollut. 247, 128–135.
Liu, R.P., Gong, W.X., Lan, H.C., Yang, T.M., Liu, H.J., Qu, J.H., 2012. Simultaneous removal of arsenate and fluoride by iron and aluminum binary oxide: competitive adsorption effects. Separ. Purif. Technol. 92, 100–105.
Liu, R.X., Guo, J.L., Tang, H.X., 2002. Adsorption of fluoride, phosphate, and arsenate ions on a new type of ion exchange fiber. J. Colloid Interface Sci. 248, 268–274.
Liu, S.B., Huang, B.Y., Chai, L.Y., Liu, Y.G., Zeng, G.M., Wang, X., et al., 2017. Enhancement of As(V) adsorption from aqueous solution by a magnetic chitosan/biochar composite. RSC Adv. 7, 10891–10900.
Luo, C.H., Tian, J., Zhu, P.L., Zhou, B., Bu, D., Lu, X.B., 2018. Simultaneous removal of fluoride and arsenic in geothermal water in Tibet using modified yak dung biochar as an adsorbent. Royal Society Open Science 5, 181266.
Ma, Y.Q., Ma, Z.H., Yin, S.Q., Yan, X.Y., Wang, J.D., 2017. Arsenic and fluoride induce apoptosis, inflammation and oxidative stress in cultured human umbilical vein endothelial cells. Chemosphere 167, 454–461.
Merodio-Morales, E.E., Reynel-Avila, H.E., Mendoza-Castillo, D.I., Duran-Valle, C.J., Bonilla-Petriciolet, A., 2020. Lanthanum- and cerium-based functionalization of chars and activated carbons for the adsorption of fluoride and arsenic ions. Int. J. Environ. Sci. Technol. 17, 115–128.
Mohan, D., Kumar, S., Srivastava, A., 2014a. Fluoride removal from ground water using magnetic and nonmagnetic corn stover biochars. Ecol. Eng. 73, 798–808.
Mohan, D., Sarswat, A., Ok, Y.S., Pittman, C.U., 2014b. Organic and inorganic contaminants removal from water with biochar, a renewable, low cost and sustainable adsorbent - a critical review. Bioresour. Technol. 160, 191–202.
Purwajanti, S., Zhang, H.W., Huang, X.D., Song, H., Yang, Y.N., Zhang, J., et al., 2016. Mesoporous magnesium oxide hollow spheres as superior arsenite adsorbent: synthesis and adsorption behavior. ACS Appl. Mater. Interfaces 8, 25306–25312.
Qiao, J.L., Cui, Z.M., Sun, Y.K., Hu, Q.H., Guan, X.H., 2014. Simultaneous removal of arsenate and fluoride from water by Al-Fe (hydr)oxides. Front. Environ. Sci. Eng. 8, 169–179.
Saikia, R., Goswami, R., Bordoloi, N., Senapati, K.K., Pant, K.K., Kumar, M., et al., 2017. Removal of arsenic and fluoride from aqueous solution by biomass based activated biochar: optimization through response surface methodology. Journal of Environmental Chemical Engineering 5, 5528–5539.
Tan, X.F., Liu, Y.G., Gu, Y.L., Xu, Y., Zeng, G.M., Hu, X.J., et al., 2016. Biochar-based nano-composites for the decontamination of wastewater: a review. Bioresour. Technol. 212, 318–333.
Thakur, L.S., Mondar, P., 2017. Simultaneous arsenic and fluoride removal from synthetic and real groundwater by electrocoagulation process: parametric and cost evaluation. J. Environ. Manag. 190, 102–112.
Vaughan, R.L., Reed, B.E., 2005. Modeling As(V) removal by a iron oxide impregnated activated carbon using the surface complexation approach. Water Res. 39, 1005–1014.
Venkateswarlu, S., Lee, D., Yoon, M., 2016. Bioinspired 2D-carbon flakes and Fe3O4 nanoparticles composite for arsenite removal. ACS Appl. Mater. Interfaces 8, 23876–23885.
Wang, S., Gao, B., Li, Y., Creamer, A.E., He, F., 2017. Adsorptive removal of arsenate from aqueous solutions by biochar supported zero-valent iron nanocomposite: batch and continuous flow tests. J. Hazard Mater. 322, 172–181.
Wang, S.S., Gao, B., Li, Y.C., 2016. Enhanced arsenic removal by biochar modified with nickel (Ni) and manganese (Mn) oxyhydroxides. J. Ind. Eng. Chem. 37, 361–365.
Wang, Y.X., Li, J.X., Ma, T., Xie, X.J., Deng, Y.M., Gan, Y.Q., 2021. Genesis of geogenic contaminated groundwater: as, F and I. Crit. Rev. Environ. Sci. Technol. 51. https://doi.org/10.1080/10643389.2020.1807452.
Wasay, S.A., Haron, J., Tokunaga, S., 1996. Adsorption of fluoride, phosphate, and arsenate ions on lanthanum impregnated silica gel. Water Environ. Res. 68, 295–300.
Xiao, X., Chen, B.L., Zhu, L.Z., 2014. Transformation, morphology, and dissolution of silicon and carbon in rice straw-derived biochars under different pyrolytic temperatures. Environ. Sci. Technol. 48, 3411–3419.
Xu, P., Capito, M., Cath, T.Y., 2013. Selective removal of arsenic and monovalent ions from brackish water reverse osmosis concentrate. J. Hazard Mater. 260, 885–891.
Zhang, M., Gao, B., Varnoosfaderani, S., Hebard, A., Yao, Y., Inyang, M., 2013. Preparation and characterization of a novel magnetic biochar for arsenic removal. Bioresour. Technol. 130, 457–462.